Laser and Particle Beams (2015), *33*, 221–236.

doi:10.1017/S0263034615000233

Pre-plasma effect on laser beam energy transfer to a dense target under conditions relevant to shock ignition

T. PISARCZYK,[1] S.YU. GUS'KOV,[2,3] O. RENNER,[4] N.N. DEMCHENKO,[2] Z. KALINOWSKA,[1] T. CHODUKOWSKI,[1] M. ROSINSKI,[1] P. PARYS,[1] M. SMID,[4,5] J. DOSTAL,[6] J. BADZIAK,[1] D. BATANI,[7] L. VOLPE,[7] E. KROUSKY,[6] R. DUDZAK,[6] J. ULLSCHMIED,[6] H. TURCICOVA,[4] J. HREBICEK,[4] T. MEDRIK,[4] M. PFEIFER,[6] J. SKALA,[6] A. ZARAS-SZYDLOWSKA,[1] L. ANTONELLI,[7] Y. MAHEUT,[7] S. BORODZIUK,[1] A. KASPERCZUK,[1] AND P. PISARCZYK[8]

[1]Institute of Plasma Physics and Laser Microfusion, Warsaw, Poland
[2]P.N. Lebedev Physical Institute of RAS, Moscow, Russian Federation
[3]National Research Nuclear University "MEPhI" (Moscow Engineering Physics Institute), Moscow, Russian Federation
[4]Institute of Physics ASCR, Prague, Czech Republic
[5]Czech Technical University, FNSPE, Prague, Czech Republic
[6]Institute of Plasma Physics ASCR, Prague, Czech Republic
[7]Université Bordeaux, CNRS, CEA, CELIA, Talence, France
[8]Warsaw University of Technology, ICS, Warsaw, Poland

(Received 2 November 2014; Accepted 9 February 2015)

Abstract

This paper reports on properties of a plasma formed by sequential action of two laser beams on a flat target, simulating the conditions of shock-ignited inertial confinement fusion target exposure. The experiments were performed using planar targets consisting of a massive copper (Cu) plate coated with a thin plastic (CH) layer, which was irradiated by the 1ω PALS laser beam ($\lambda = 1.315$ μm) at the energy of 250 J. The intensity of the fixed-energy laser beam was scaled by varying the focal spot radius. To imitate shock ignition conditions, the lower-intensity auxiliary 1ω beam created CH-pre-plasma which was irradiated by the main beam with a delay of 1.2 ns, thus generating a shock wave in the massive part of the target. To study the parameters of the plasma treated by the two-beam irradiation of the targets, a set of various diagnostics was applied, namely: (i) Two-channel polaro-interferometric system irradiated by the femtosecond laser (~40 fs), (ii) spectroscopic measurements in the X-ray range, (iii) two-dimensional (2D)-resolved imaging of the K_α line emission from Cu, (iv) measurements of the ion emission by means of ion collectors, and (v) measurements of the volume of craters produced in a massive target providing information on the efficiency of the laser energy transfer to the shock wave. The 2D numerical simulations have been used to support the interpretation of experimental data. The general conclusion is that the fraction of the main laser beam energy deposited into the massive copper at two-beam irradiation decreases in comparison with the case of pre-plasma. The reason is that the pre-formed and expanding plasma deteriorates the efficiency of the energy transfer from the main laser pulse to a solid part of the targets by means of the fast electrons and the wave of an electron thermal conductivity.

Keywords: Energy transport; Fast electrons; Femtosecond interferometry; Laser-produced plasma; Shock ignition

1. INTRODUCTION

Shock ignition (SI) approach (e.g., Scherbakov, 1983; Betti *et al.*, 2007; Perkins *et al.*, 2009; Ribeyre *et al.*, 2009; Batani *et al.*, 2014*b*) is actually one of the most promising methods for target ignition in inertial confinement fusion (ICF). Requirements for SI concept are not easy to obtain: pressure of igniting shock wave excited by the laser spike action on the ICF target preliminary compressed to the density of 10 g/cm^3 should not be lower than 300 Mbar and at the same time, the laser spike intensity and duration should vary in quite narrow ranges of 1–10 PW/cm^2 and 200–500 ps. One of the main research aims related to the SI concept is the investigation of the ablation pressure mechanism due to the above-mentioned laser and target parameters. SI conception reckons that a significant part of the absorbed laser energy is converted to fast electrons under

Address correspondence and reprint requests to: Tadeusz Pisarczyk, Institute of Plasma Physics and Laser Microfusion, 23 Hery St., 01-498 Warsaw, Poland. E-mail: tadeusz.pisarczyk@ifpilm.pl

the presence of the pre-plasma. The energy transfer by fast electrons into the plasma with supercritical density can generate an ablation pressure of several hundreds of Mbar, which is necessary for producing the igniting shock (Gus'kov *et al*., 1983; 2012; Antonelli *et al*., 2011). Recent experiments with OMEGA laser (Theobald *et al*., 2008; 2012) seem to suggest an increasing efficiency of the energy transfer to both planar and spherical targets, resulting from the contribution of fast electrons generated due to stimulated Raman scattering and two-plasmon decay in an extended pre-plasma.

The role of fast electrons in the laser energy conversion to shock waves was also investigated in our previous research (Gus'kov *et al*., 2004; 2014; Kalinowska *et al*., 2012; Koester *et al*., 2013; Batani *et al*., 2014*a*) performed with the PALS iodine laser. At the beginning, massive targets of Al and Cu have been irradiated at various focal spot radii of the fundamental frequency (1ω) and frequency-tripled (3ω) laser beam radiation to identify the mechanisms of the laser absorption and to determine their influence on the absorbed energy transfer to the target (Gus'kov *et al*., 2004; 2014; Kalinowska *et al*., 2012). It was shown that the fast electrons generated due to resonant absorption gave a main contribution to ablation pressure at the first harmonic irradiation, whereas the usual mechanism of ablation by thermal conductivity wave occurred at the third harmonic irradiation. The mass of the ablated solid material and the fraction of the laser energy deposited in the plasma have been determined, respectively, using the three-frame interferometer and by measuring the volume of the crater created on the solid surface. Hitherto the interferometric system was irradiated by the 2nd or 3rd harmonic of the iodine laser featuring approximately 250 ps pulse, identical by its duration to the main plasma generating laser pulse. With such relation between the diagnostic and the main laser pulse duration, this system could not allow for sufficiently detailed plasma probing. Expansion velocities corresponding to the fast component of the ablation plasma generated in the initial stage of the plasma expansion are of the order of 10^8 cm/s. Under such conditions blurring of interference fringes close to the critical density region, caused by plasma movement and/or oscillations, did not allow to measure the maximal reachable ion density governed by the diagnostic laser wavelength. To remedy this, a two-channel polaro-interferometric system irradiated by the femtosecond laser with the pulse duration of ~40 fs was implemented as the main optical diagnostic to investigate the laser-produced plasma at PALS. The use of this diagnostic system allowed us to obtain electron density distributions with much better temporal resolution, sufficient to record interferograms of the early stages of expansion, by effective sampling through duration of the plasma-generating laser pulse.

The experimental results presented here shed more light on effects of laser-produced fast electrons under the presence of pre-created extended plasma that is relevant to SI conditions. The pre-plasma was created by the action of the laser pulse with a relatively low intensity. This pulse preceded the high intensity, 1ω laser pulse which produced high-energy fast electrons. The comparison of the properties of one- and two-beam irradiated plasmas was based on measurements including interferometric investigation of the electron density distribution, X-ray spectroscopic measurements of the plasma temperature and density near the ablation surface, two-dimensional (2D) imaging of the fast electron spreading via K_α emission, ion emission measurements using the ion detectors, and measurements of the volume of craters produced on the target surface.

The coupling parameter $I\lambda^2$ (I is the intensity of laser radiation and λ is the laser radiation wavelength) in the experiments with small radii beam exceeded the value of, approximately, 10^{15} W μm^2/cm^2, when the fast electron generation occurs as the result of development of the parametric instabilities. However, under single-beam irradiation by relatively short PALS laser pulse, the laser-produced plasma is not enough extended to wait the contribution of parametric instabilities to the laser energy conversion into fast electron energy comparable with resonant absorption. The results of the previous experiments with one-beam irradiation (Gus'kov *et al*., 2014) are in a good agreement with numerical simulations, where the generation of fast electron due to resonant absorption and their transport were modeled. Under two-beam irradiation the main beam interacts with the pre-plasma, when the role of parametric instabilities may be expected larger in comparison with the one-beam irradiation case. At the same time, the numerical simulation modeling of the experiment presented below shows that under two-beam irradiation the contribution of resonant absorption significantly increases in comparison with the one-beam case. The absorption coefficient of the resonant mechanism reaches the level of 20–30%. For this reason, we remain in the conviction that under two-beam irradiation the resonant absorption makes a predominant contribution to the fast electron generation, too. As in our previous investigations, 2D numerical simulations (2DSs) by the ATLANT-HE code (Lebo *et al*., 2004) and an analytical model (Gus'kov *et al*., 2004) which include fast electron generation by resonant absorption and their transport have been applied for the interpretation of experimental data.

In comparison with our previous papers (Gus'kov *et al*., 2014; Pisarczyk *et al*., 2014), here we report the results benefitting from the application of modified complex diagnostics which provide additional knowledge on the role of fast electron energy transfer in the process of the plasma production under the conditions of one- and two-beam laser irradiation.

The paper is structured as follows. In Section 2, the experimental setup is described. The results concerning the investigation of efficiency of laser energy transfer to solid target via interferometric and crater measurements are presented in Section 3. Sections 4 is dedicated to X-ray spectroscopy and imaging measurements, whereas Section 5 summarizes the ion emission studies. Section 6 brings the results of numerical simulations. Finally, Section 7 summarizes the results obtained.

https://doi.org/10.1017/S0263034615000233 Published online by Cambridge University Press

2. EXPERIMENTAL SETUP

The interferometric investigation of the ablative plasma with the femtosecond resolution and the measurements of the crater creation efficiency were the main source of information about the laser energy transport process to the shock wave generated in the solid target. Similar to (Koester *et al.*, 2013; Batani *et al.*, 2014*a*; Pisarczyk *et al.*, 2014), the experiments were performed using Cu massive planar targets covered by 25 μm plastic layer (C_8H_7Cl), which were irradiated by the 1ω laser beam ($\lambda = 1.315$ μm) at the energy of 250 J. Structure and irradiation geometry of the two-layer target are presented in Figure 1.

To imitate the SI conditions, the lower-intensity auxiliary 1ω beam with the energy of ~40 J and angle of incidence $\alpha = 25°$ created CH-pre-plasma that was irradiated by the main beam with a delay of 1.2 ns, thus generating the shock wave in the massive part of the target.

Both beams were equipped with phase plates to generate homogeneous irradiation of the target surface. Due to the phase plate, the minimal focus spot radius on the target was larger by about 10 μm compared with the case without it. Therefore, the investigations were carried out at different intensities of the main 1ω beam controlled by the varying focal spot radius in a range of 50–200 μm and keeping the laser energy fixed.

To determine the influence of the pre-plasma on the investigated process, the interferometric data were complemented by additional diagnostics:

- X-ray spectrometer with one-dimensional (1D) spatial resolution allowing determination of the effective electron temperature and density of the ablative plasma;
- The 2D imaging of the fast electron distribution based on detection of the Cu K_α line emission using the spherically bent quartz crystal; and
- ion grid collectors to measure the ion emission as an additional source of information about the thermal electron temperature, the average fast electron energy as well as the geometry of expansion of the ablative plasma.

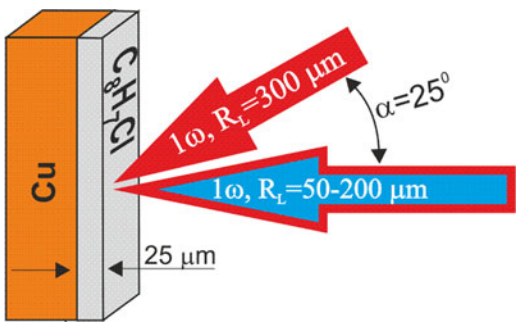

Fig. 1. The structure and geometry of irradiation of the two-layer target.

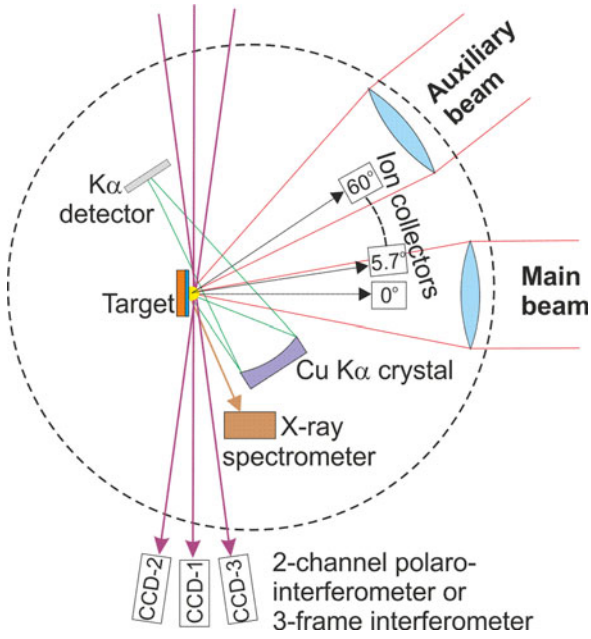

Fig. 2. Schematic configuration of diagnostics used in the experiment.

The configuration of the diagnostics used in the PALS experiment is shown in Figure 2.

3. INTERFEROMETRIC AND CRATER VOLUME MEASUREMENTS

3.1. Femtosecond Interferometry Results

Interferometric measurements were realized by means of the two-channel polaro-interferometer which provides a possibility to register two interferometric frames with the variable time delay in the range of 0–1000 ps; see Figure 3. To irradiate this system, PALS Ti:Sa femtosecond laser with the wavelength 0.8 μm and the pulse duration ~40 fs was used. Each channel of the polaro-interferometer was equipped with a charge-coupled device camera (RM-4200 GigEV) enabling registration of interferograms with the high spatial resolution (2048 × 2048 pixels with a size of ~6 μm) and the 16-bit dynamics. Cameras are connected to a computer through a Gigabit ethernet interface and controlled by a custom-built application PALS Vision GigEV, which is capable of pretreatment of the images (modification of the Fourier spectra, correction of histograms, correction of colors, calibration, etc.). In the case of high-quality interferograms, electron density distribution may be obtained after the laser shot with *on-the-fly* mode. For more detailed analysis of interferograms, a specialized software (created at IPPLM) is used.

The interferometric records were taken in the time periods chosen with respect to the full width at half maximum of the main laser pulse, that is, about 350 ps. Two-frame sequences of interferograms with the time separation between frames about 430 ps were recorded within the range from −100 to

https://doi.org/10.1017/S0263034615000233 Published online by Cambridge University Press

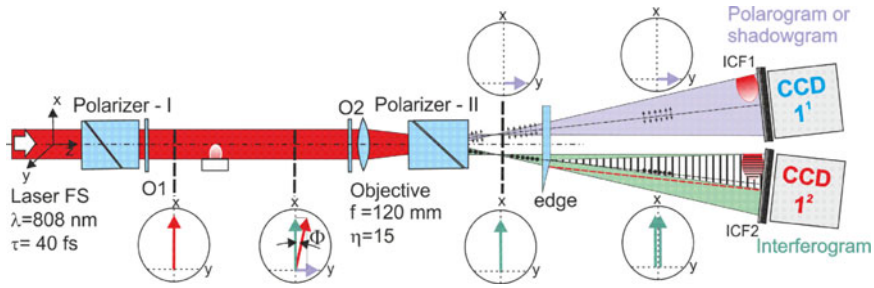

Fig. 3. Optical scheme of the polaro-interferometer channel.

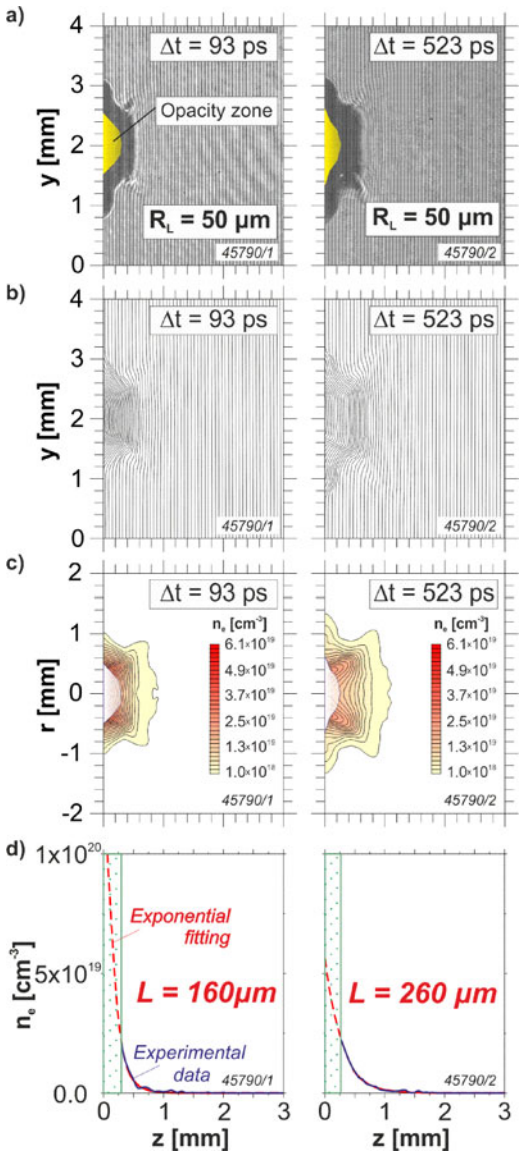

Fig. 4. Raw interferograms (a), their reconstruction (b), electron density distributions (c), and the axial electron density distributions (d) illustrating the ablative plasma expansion during the laser pulse interaction. The records correspond to the minimum focal spot radius and the pre-plasma absence (only the main beam was used).

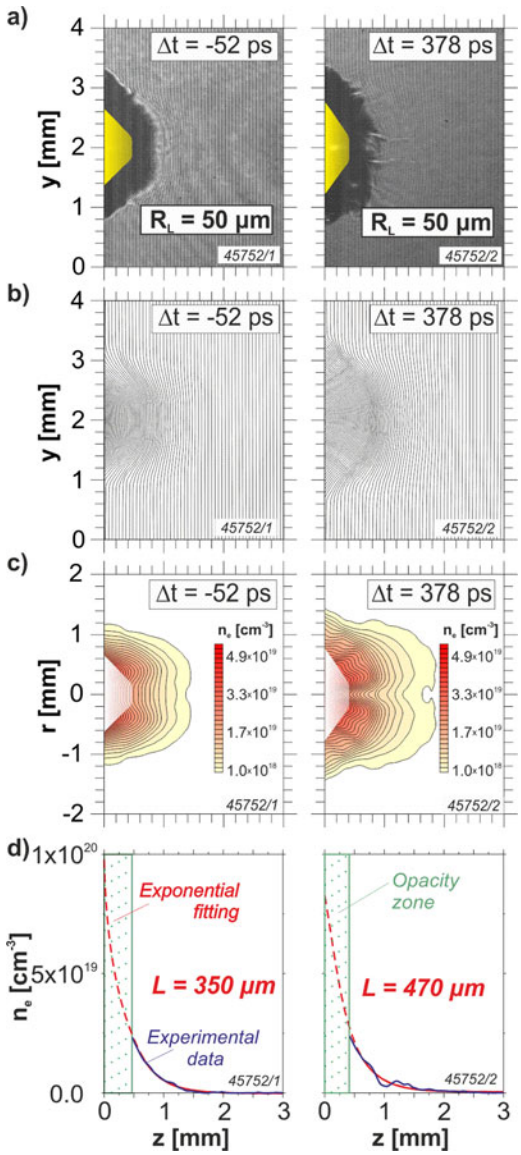

Fig. 5. Raw interferograms (a), their reconstruction (b), electron density distributions (c) calculated on the basis of the reconstructions, and the axial electron density distributions (d) illustrating the ablative plasma expansion during the laser pulse interaction at the minimum focal spot radius in the case of the pre-plasma presence.

https://doi.org/10.1017/S0263034615000233 Published online by Cambridge University Press

1000 ps related to the maximum intensity of the main laser pulse. The sample sequence of interferograms illustrating the ablative plasma expansion during the laser pulse interaction is presented in Figure 4a.

The recorded sequence of the interferograms for different time delays enabled us to obtain the detailed information about time evolution of the electron density distribution in the ablative plasma during the laser pulse interaction with the targets. To calculate the electron density distribution, phase distribution was determined on the basis of the reconstructed interferograms (Fig. 4b) using *maximum-of-a-fringe* method. The reconstruction included also the opacity zone (both in and outside axial region), where phase was extrapolated (Kasperczuk & Pisarczyk, 2001). To solve the Abel equation, Fast Fourier Transform was applied (Kalal & Nugent, 1988; Burrus, 2008). In the case of the pre-plasma absence, the axial asymmetry does not exceed 10% and the inaccuracy of determination of the shifts of the fringes in the area outside the opacity zone is relatively low (several percent only), therefore this method of the Abel equation solution gives the accuracy of the electron density determination with error about 20%.

To obtain the information about the density gradient scalelength, an exponential fitting of the experimental axial density profiles has been applied: $n_e(z) = n_0 e^{-z/L}$. The parameters of this function determine the maximum electron density gradient in the opacity zone: $[dn_e/dz]_{z=0} = n_0/L$, where L is the scalelength of the density gradient and n_0 is the maximum electron density. The electron density distributions calculated on the basis of interferograms from Figure 4a are shown in Figure 4c. The fitting of the axial density profile by the exponential function is shown in Figure 4d.

The sample sequence of interferograms, corresponding electron density distributions and axial profiles of the electron density illustrating the ablative plasma expansion during the laser pulse interaction in the presence of the pre-plasma (both auxiliary and the main beam were applied) are presented in Figure 5. The comparison of the electron density distribution of the ablative plasma obtained under the absence of the pre-plasma at different focal spot radii and for different time of the plasma stream expansion is presented in Figure 6.

Axial density profiles and the scalelength corresponding to these distributions are shown in Figure 7. The time delays of each individual frame relate to the maximal intensity of the main pulse. The electron density distributions presented in Figure 6 demonstrate the quasi-spherical character of the expansion for the small focal spot radius with the characteristic

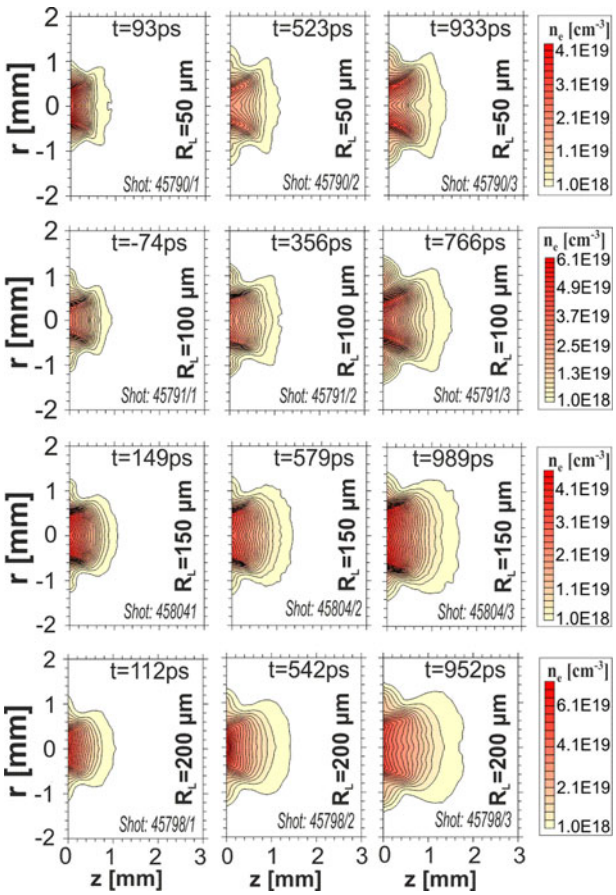

Fig. 6. Density distributions illustrating the time evolution of the ablative plasma expansion for different focal spot radii in the case of the pre-plasma absence.

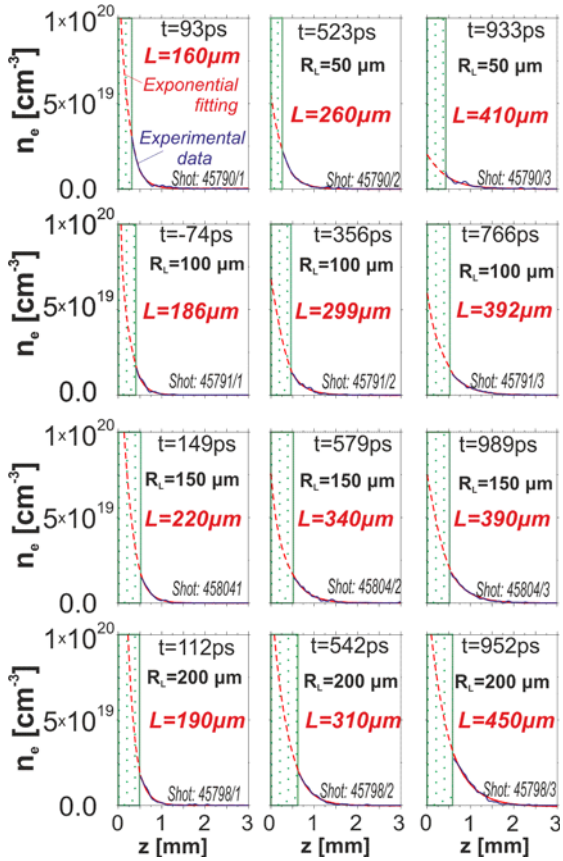

Fig. 7. Axial density profiles and the scalelength characterizing the ablative plasma expansion during the laser pulse interaction for different focal spot radii in the case of the pre-plasma absence.

https://doi.org/10.1017/S0263034615000233 Published online by Cambridge University Press

minimum of the density on the axis. When increasing the focal spot radius of the laser beam, the plasma stream expansion becomes more axial. It is seen from both the time sequence of the density distributions, Figure 6, and the axial profiles, Figure 7, related to larger focal spot radii: R_L = 150 and 200 μm. This change in the character of the ablative plasma expansion (from spherical to axial) caused by the increasing focal spot radius and the relevant scalelengths are demonstrated in Figure 7. In the case of the pre-plasma presence, the time sequences of the electron density distribution of the ablative plasma obtained for different irradiation conditions are shown in Figure 8. The electron density distributions indicate that the light plasma with the higher pressure, being generated from the thin plastic layer by auxiliary beam, limits the radial expansion of the central plasma created by the main laser beam. The radial limitation favors the axial character of the plasma expansion particularly in the case of the larger focal spot radii. The radial limitation results in the growth of the electron density on the axis and in the increase of the scalelength. This is clearly demonstrated by the axial density profiles and the scalelength values in Figure 9. In contrast, when the pre-plasma is not created, the scalelength of the ablative plasma is considerably smaller. The detailed comparison of the ablative plasma expansion

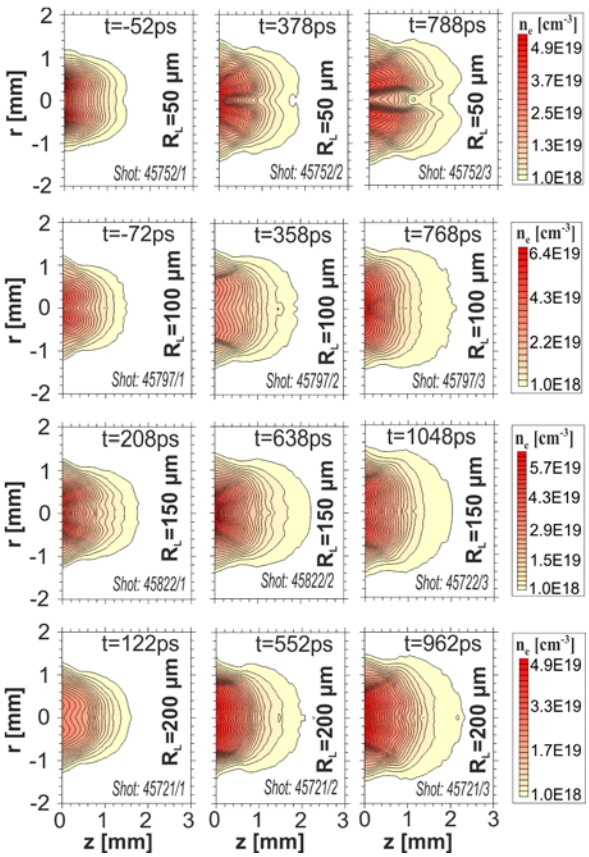

Fig. 8. Electron density distributions illustrating the time evolution of the ablative plasma expansion during the laser pulse interaction with the target at different focal spot radii under the presence of the pre-plasma.

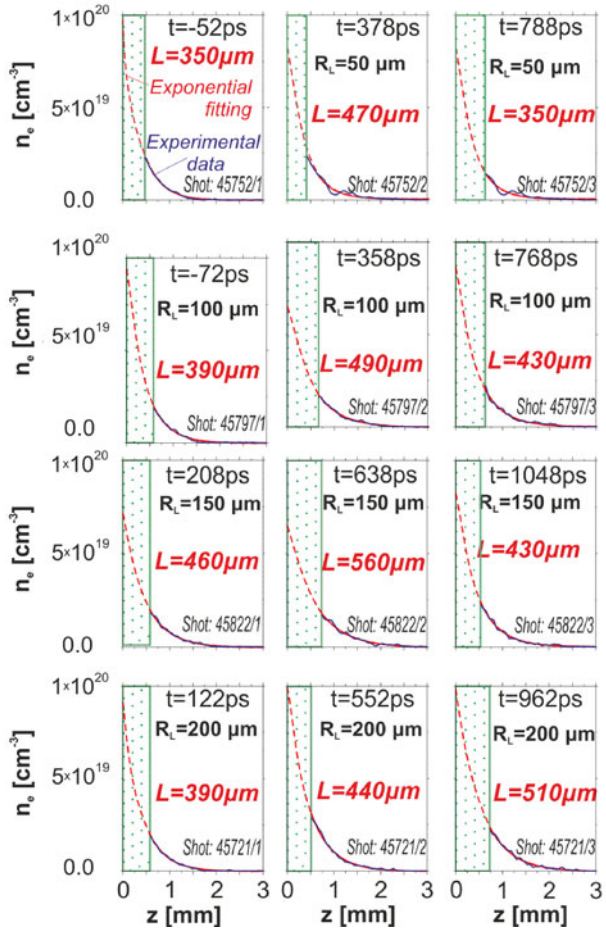

Fig. 9. Axial density profiles and the scalelength characterizing of the ablative plasma expansion during the laser pulse interaction at different focal spot radii in the case of the pre-plasma presence.

in the case of absence and presence of the pre-plasma is presented in Figure 10. This figure shows the maximal density gradient, the scalelength and the maximal density for three characteristic times of the expansion: 0, 200, and 600 ps related to the maximum intensity of the main laser beam. Single values corresponding to chosen expansion times have been determined by approximating the experimental data. Figure 10a shows that in the case without the pre-plasma, the density gradient increases with the decreasing R_L for the focal spot radii smaller than 150 μm. The largest growth of the density gradient corresponds to the maximum laser pulse intensity ($t = 0$). The density gradient achieves value about 1×10^{22} cm^{-4} for the minimum focal spot radius ($R_L = 50$ μm) and this gradient corresponds to the minimal scalelength $L = 160$ μm. It can be explained that for the time of the ablative plasma expansion $t = 0$, the favorable conditions for high energy fast electron generation due to resonant absorption occur. This effect is responsible for the energy transfer to the shock wave generated in a solid target. As follows from Figure 10a, the density gradient also increases with increasing the focal spot radii above 150 μm. However, this growth is connected with passage

https://doi.org/10.1017/S0263034615000233 Published online by Cambridge University Press

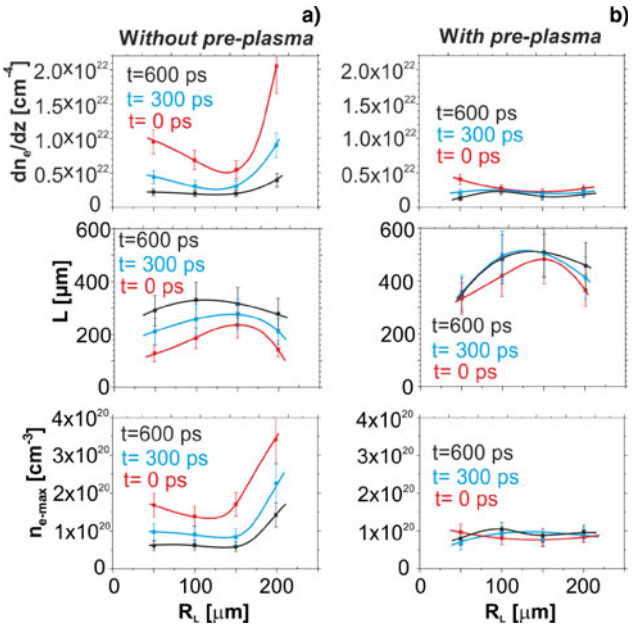

Fig. 10. Comparison of the maximal density gradient, the scalelength, and the maximal electron density following from interferometric fitting obtained in the case of (a) absence and (b) presence of the pre-plasma.

to predominating 1D expansion of the ablative plasma at large focal spot radii (Gus'kov *et al.*, 2014).

In the case of the pre-plasma presence, Figure 10b, the density gradient falls in the whole range of the focal spot radii and the expansion time includes the maximum intensity of the laser pulse and ensuing 600 ps. The scalelength is increased by approximately two times as compared with the case with the pre-plasma absence. At the maximum laser intensity $t = 0$ and the minimal focal spot radius $R_L = 50$ μm, the scalelength grows to the level of about $L = 330$ μm. This proves that under the presence of the pre-plasma, the effect of the energy transfer by fast electrons becomes smaller. The presence of the extended pre-plasma leads to decreasing density gradients of the plasma created by the action of the main beam.

3.2. Crater Volume Measurements

In our previous papers (Kalinowska *et al.*, 2012; Gus'kov *et al.*, 2014; Pisarczyk *et al.*, 2014), it has been shown that the interferometric measurements in combination with the crater volume analysis can provide essential information about mechanisms of the laser radiation absorption. The ratio N/V_{cr} (where N is the total electron number in the plasma plume and V_{cr} is the crater volume in cm^3) defines a number of thermal electrons participating in the creation of crater volume unit (1 cm^3).

To calculate the total electron number (N) in the ablative plasma the following formula was used:

$$N = 2\pi \int_0^R \int_0^Z n_e(r, z)\, r\, dr dz \tag{1}$$

where $n_e(r, z)$ is the electron density distribution obtained from the interferometric measurements [after reconstruction of interferograms (Kasperczuk & Pisarczyk, 2001)] including electrons inside and outside the opacity zone. The way of the crater volume determination is presented in our previous paper (Pisarczyk *et al*, 2014). The N/V_{cr} parameter was evaluated only for expansion time: $t = 600$ ps, that is, after the end of main laser pulse, when both ablation process and processes related to absorption of laser radiation were completed. Figure 11 presents a comparison of the crater volumes V_{cr}, total electron number N, and N/V_{cr} parameter obtained for the target irradiation without and with the pre-plasma.

The rate of increase of the number of plasma electron in the approximation of the axial expansion is determined by the flow of electrons from the surface with the critical plasma density, where the main part of the laser radiation is absorbed:

$$\frac{dN}{dt} = n_{cr} C_s \pi R_L^2 \tag{2}$$

Here $n_{cr} = 1.12 \times 10^{21}/\lambda^2$ is the critical electron concentration measured in cm^{-3} for the light with the wavelength λ given in μm, C_s is the sound velocity of the plasma near the critical surface:

$$C_s = \left[\frac{2(\gamma - 1)}{3\gamma - 1} \frac{K_{ab} I_L}{\rho_{cr}}\right]^{1/3} \tag{3}$$

where $\rho_{cr} = A m_p n_{cr}/Z$ is the critical plasma density, m_p is the proton mass, A and Z are the ion atomic number and charge, K_{ab} is the absorption coefficient, I_L and R_L are the laser

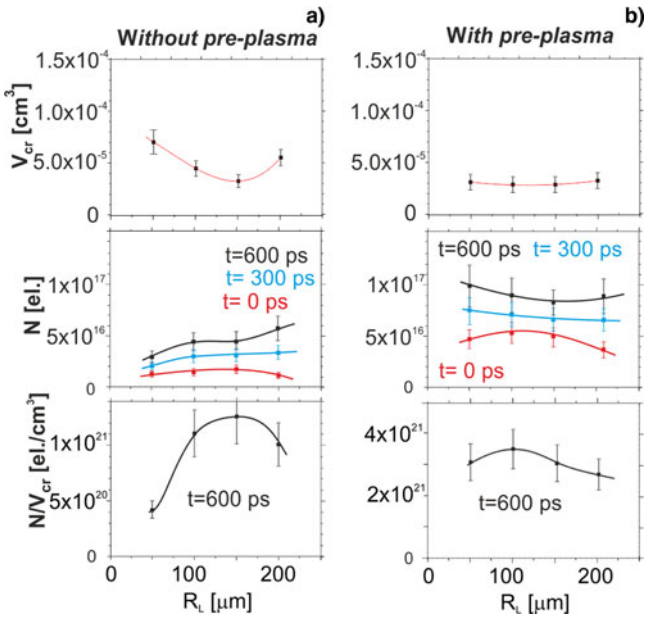

Fig. 11. Comparison of the crater volumes V_{cr}, the total electron number N, and the N/V_{cr} parameter obtained in the case of (a) absence and (b) presence of the pre-plasma.

https://doi.org/10.1017/S0263034615000233 Published online by Cambridge University Press

intensity and beam radius, respectively. Substituting expression (3) into Eq. (2) and assuming the plasma is a perfect totally ionized gas, we have:

$$\frac{dN}{dt} = 2.1 \times 10^{27} \lambda^{4/3} R_L^{4/3} \left[\frac{K_{ab} E_L(\mathrm{J})}{\tau_L(\mathrm{ns})} \right]^{1/3} \quad (4)$$

Here the laser energy E_L(J), pulse duration τ_L(ns), beam radius R_L, and λ are measured in Joule, ns, cm, and μm, respectively.

This simple evaluation gives an explanation of the measurements of the thermal electron number of the plasma torch. For $E_L = 250$ J, $\tau_L = 0.3$ ns, $\lambda = 1.351$ μm, $R_L = 100$ μm, and absorption coefficient $K_{ab} \approx 0.3$, the rate dN/dt is approximately 4.5×10^{25} electrons per second. The rate dN/dt which can be concluded from the data of Figure 11a is approximately 5×10^{25} that is very close to the theoretical evaluation. For the time $t = 0$, that is, for the maximum of laser pulse, the rate of 4.5×10^{25} provides the number of electrons close to 7×10^{15} and three times larger number for the time $t = 300$ ps. It is to be noted that at approximately the same experimental and calculated rates of the electron number growth, the measured number of electrons is larger by a factor of 1.4 than the theoretical estimates. It can be explained by the fact that in the experiment, the plasma creation occurs during the time period including the pre-pulse.

In the case of the pre-plasma absence, Figure 11a, the crater volumes and the N/V_{cr} parameter demonstrate the increased efficiency of the crater creation with the decreasing focal spot radius in the range of $R_L < 150$ μm. According to our previous papers (Gus'kov *et al.*, 2014; Pisarczyk *et al.*, 2014), this corresponds directly to the energy transfer into the target by fast electrons generated due to resonant absorption. However, the crater creation efficiency also grows in the range of the focal spot radii larger than $R_L = 150$ μm. When the beam radius exceeds this value, the fast electron temperature decreases (with decreasing the laser intensity) and the role of the fast electron energy transfer in the ablation process becomes smaller than the role of thermal conductivity. In this case, the crater volume growth is due to decreasing the transverse expansion of the laser-produced plasma. It is confirmed by interferometric results, which show the increasing density gradient (see Figure 10a) that is connected with the axial (1D) expansion of the ablative plasma, which predominates in the case of the 1ω radiation and $R_L > 150$ μm. The transverse plasma expansion decreases, the pressure increases and, hence, the efficiency of the energy transformation to the shock wave also increases. According to Borodziuk *et al.* (2004), the largest crater in the massive Cu target is created by means of the 1ω laser beam focused to the focal spot radius about 300 μm.

At the pre-plasma presence, Figure 11b, the crater volume decreases to the level about 3×10^{-5} cm^{-3}, and this value does not depend on the focal spot radius of the main laser beam. Comparison with Figure 11a indicates that in the presence of pre-plasma, the effect of the fast electron energy transfer to the solid target is suppressed.

The experimental data stating the rate of the electron number growth in the presence of the pre-plasma (Figure 11b) are approximately by a factor of 1.5 larger in comparison with the case of the pre-plasma absence. It can be explained by the fact that in this case the absorption coefficient [see Eq. (3)] according to the results of numerical simulation presented below is twice higher than in the case of the pre-plasma absence. The rate of 8×10^{25} electrons per second can provide the number of electrons equal to approximately 1.2×10^{16} and 3.6×10^{16}. These values are about twice smaller than the data of Figure 11b which is ascribed to the contribution of the electrons from the pre-plasma.

To conclude, according to the temporary changes of the gradient determined from interferometric measurements the temporal changes of the N/V_{cr} parameter confirm that electrons produced in time $t = 0$ provide the largest contribution to the creation of the craters, corresponding to the maximum of the main laser pulse intensity.

4. X-RAY MEASUREMENTS

4.1. X-ray Spectroscopy Measurements

To obtain information about the electron temperature in the ablative plasma, a spectrometer with the spherically bent crystal of mica was applied. As mentioned above, the Cu massive targets were coated with 25 μm-thick layer of plastic containing chlorine (parylene-C and C_8H_7Cl). The Cl He_α and Ly_α emission were measured in the 4th spectroscopic order, whereas the He_δ and Ly_β emission in the 5th order. The spectra were observed at an angle of 11.5° from the target surface and they were recorded on X-ray film Kodak Industrex AA400. The spatial resolution of the spectroscopic geometry used was 10 μm. Typically, the recorded spectra were intentionally saturated in the He_α region to increase the signal intensity for diagnostically important He_δ and Ly_β lines which were used for evaluation of the effective plasma parameters. The exposed films were digitized using a scanner with spatial resolution of 5.3 μm and the recorded signal was recalculated to incident photon fluxes via known characteristics of the scanner and X-ray film. The spectra were further corrected with respect to the wavelength-dependent crystal reflectivity and filter transmission. The wavelength calibration was done by using the ray-traced dispersion relation and tabulated wavelengths of the dominant X-ray lines. The evaluated spectra correspond to the emission from plasma regions close to the center of the focal spot on the laser-irradiated target surface.

To determine the effective plasma parameters, the measured spectra were fitted with synthetic spectra calculated by the PrismSpect code (MacFarlane *et al.*, 2007) using the steady-state approximation. This model is dependent on three parameters: Effective plasma temperature T, density ρ, and size L. The plasma size L has been estimated by

https://doi.org/10.1017/S0263034615000233 Published online by Cambridge University Press

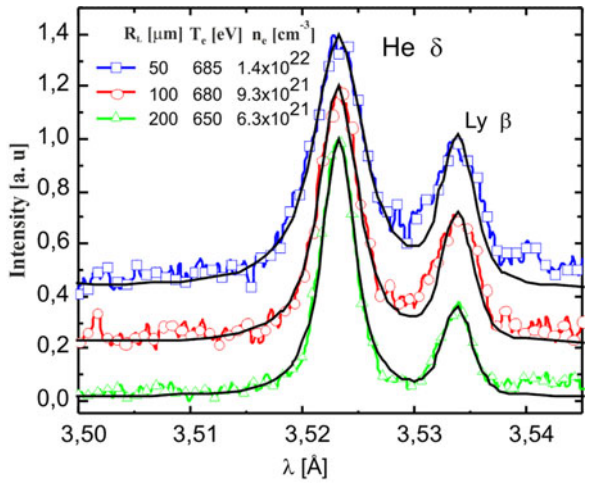

Fig. 12. The line profiles of the Cl He_δ and Ly_β lines measured for the different focal spot radius of the laser beam and their numerical fitting by the PrismSpect code (MacFarlane *et al.*, 2007).

using the Cl He_α line which undergoes strong opacity broadening thus being very sensitive to L. The remaining two plasma parameters, T and ρ, were evaluated for each shot using a previously described fitting procedure (Smid et al., 2013). The spectra fitting converged relatively fast, especially because the thickness of He_δ is highly sensitive to the plasma density and the ratio of He_δ and Ly_β varies with its temperature. The uncertainty estimates following from the procedure used amount to 5 eV for the plasma temperature and 10% for its density. The typical experimental spectra and their numerical fitting by the above-mentioned procedure are presented in Figure 12. They show dependences of the intensity of the He_δ and Ly_β lines on various conditions of the target irradiation. These three experimental spectra (colored lines, each tenth measured point depicted by a symbol) along with their best fits (black lines), all normalized with respect to the He_δ intensity, demonstrate the contingency between spectroscopic data and the plasma parameters. When going from the green via red to blue line, the characteristic gradual broadening (FWHM) of the He_δ profile is related to the increasing plasma density.

Similarly, the increase of the plasma temperature is connected with the increased intensity of the Ly_β line with respect to the He_δ emission. Figure 13 shows the dependence of the effective plasma density and temperature, as determined from the time-integrated X-ray emission, on the intensity of the main laser beam. These values characterize the density and temperature of plasma torch in the 100 μm-thick plasma region near the ablation surface. The real incident intensity was calculated from the measured beam energy and the focal spot radius estimated from the streak camera records.

The data are plotted using the logarithmic scale for laser intensity axis, four vertical lines correspond to the nominal interaction parameters, that is, to the energy of 240 J focused to focal spot radii $R_L = 200$, 150, 100, and 50 μm. The shown points and lines correspond to the shots performed

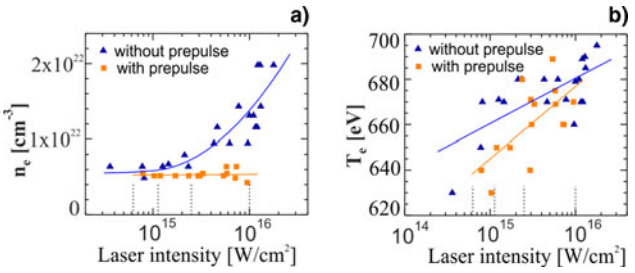

Fig. 13. Dependences of (a) the electron density and (b) the temperature on the laser intensity at the absence and presence of the pre-plasma. The parameters correspond to the 100 μm-thick plasma region at the focal spot center on irradiated targets.

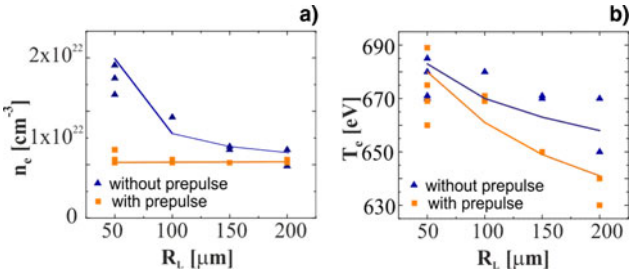

Fig. 14. Near-surface electron density (a) and temperature (b) as a function of the focal spot radius at the absence and presence of the pre-plasma.

without (blue) and with (orange) the pre-pulse. The density fit is approximated by a linear regression, while the temperature fit is a logarithmic curve (we emphasize that the laser intensity is depicted in the logarithmic scale). Figure 14 shows analogous plasma parameters plotted with respect to the nominal R_L. The plotted points correspond to the intersection of the fitted curves shown in Figure 13 with vertical lines marking nominal intensities. In addition, results for shots with R_L and the laser energy closest to the nominal values are also introduced. Figures 13 and 14 demonstrate that despite obvious shot-to-shot fluctuation, several distinct trends are clearly seen. The temperature decreases with the increasing focal spot radius (i.e., it grows with the laser intensity), both under the absence and, slightly less, under the presence of the pre-pulse. On the other hand, the observed dependences of the plasma density are significantly influenced by the presence of the pre-pulse.

It should be underlined, that the spectroscopically determined trends observed in the electron density deduced from spectroscopic measurements (cf. Figs 13 and 14) are very similar to those obtained from interferometry, despite some quantitative differences. For cases without the pre-pulse and the focal spot radii ranging from $R_L = 50$ μm to 150 μm, the electron densities determined by both methods decrease almost identically (about two times). The differences between spectroscopic and interferometric measurements relate to the R_L range larger than 150 μm and the expansion time close to $t = 0$. Here the electron density obtained from interferometry increases because of the predominating axial plasma expansion. This incompatibility is due to the fact

https://doi.org/10.1017/S0263034615000233 Published online by Cambridge University Press

that spectroscopy gives information about the effective value of the electron density averaged over time.

The presence of the pre-plasma clearly reduces the electron density which decreases to the same level for all focal spot radii. Namely, the value of ablation density determines the efficiency of the energy transfer from high-temperature plasma to non-evaporated part of the target by means of the shock wave. The ratio η of the energies of the shock wave E_s and the plasma plume E_P is determined by the ratio of the energy fluxes in the shock wave q_s and the plasma plume q_p at the ablation surface. In the plane approximation, the fluxes q_s and q_p are $P_s w_s$ and $P_a w_a$, respectively. Here the pressure behind the shock wave P_s is close to the ablation pressure P_a (the pressure at the ablation front, that is, at the border between the plasma plume and the target), and the ablation and shock wave velocities are $w_a \approx (P_a/\rho_a)^{1/2}$ and $w_s \approx (P_s/\rho_s)^{1/2}$, respectively ($\rho_a$ is the ablation density). Consequently the efficiency of the energy transformation to the shock wave increases with the increasing ablation density as $\eta \approx (\rho_a/\rho_s)^{1/2}$ (Gus'kov *et al.*, 2007).

Summarizing the results of the spectroscopic measurements, we can formulate two important conclusions:

- Without the pre-plasma, a sharp increase in ablation density with the focal spot radius decreasing from 100 to 50 μm indicates the effect of the fast electron energy transfer into the deeper region of the plasma larger than that provided by thermal conductivity. This conjecture is supported by interferometric measurements. Both X-ray spectroscopy and interferometric results confirm the conclusion that increasing efficiency of the energy transfer with the decreasing beam radius (which follows from measurements of the crater volume) results from increasing the ablation density due to the effect of fast electron energy transfer.
- The presence of the pre-plasma leads to suppression of the effect of fast electron energy transfer.

4.2. 2D Imaging of the Cu K_α Line Emission

The Cu K_α images were taken using a spherically bent crystal of quartz (422) which was set up as an imaging mode monochromator (with the Bragg angle $\theta = 88.2°$) to provide a quasi-monochromatic distribution of the K_α emission, 2D-spatially resolved along the target surface. The time-integrated K_α signals were again registered on the Kodak AA400 film. The recorded images were digitized using a calibrated table-top scanner, recalculated to optical densities and, by using the characteristic curve of the film, to intensities of the impinging radiation. The 2D-spatially resolved records contain information on emitting area and intensity of the K_α emission.

The images of the Cu K_α emission under conditions of the two-layer target irradiation (see Fig. 1) were recorded in laser shots with the absence of pre-pulses only. Typical images obtained when focusing the laser beam to focal spots with radii

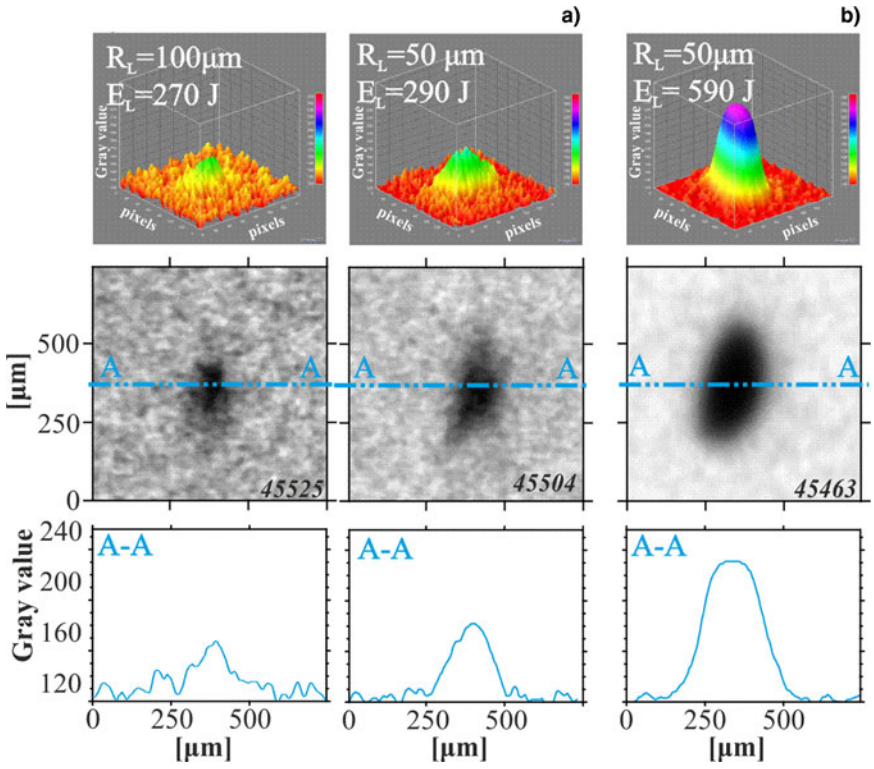

Fig. 15. Images of the Cu K_α emission registered without the presence of the pre-plasma using the minimal focal spot radii and the laser energy: (a) 290 J and (b) 590 J.

https://doi.org/10.1017/S0263034615000233 Published online by Cambridge University Press

$R_L = 50$ μm and $R_L = 100$ μm are presented in Figure 15. The intensity of the K_α signal obviously grows with the decreasing focal spot size and with the increasing energy of the laser beam. The K_α images provide direct information on the lateral range of the hot electron propagation. After subtracting the background from the detected signal, the number of photons registered over the active detector area was recalculated to the Cu K_α emission from the target benefitting from the results of ray-tracing code (Podorov *et al.*, 2001; NIST ESTAR database; Morace & Batani, 2010). With respect to relevant geometric factors (source-to-crystal-to-detector distance, crystal and detector dimension), crystal reflectivity, and transmission of the radiation through protective foils, the number of K_α photons $N_{K\alpha}$ emitted by the source into the full solid angle is related to the number of photons striking the detector by a factor of $1/3.74 \times 10^{-7}$. The results of the measurements of number of K_α photons for different focal spot radii and various laser energies are presented in Table 1. The growth of the emitted K_α photons with the increasing laser intensity demonstrates the growth of fast electron population. Taking into account our recent papers (Gus'kov *et al.*, 2014; Pisarczyk *et al.*, 2014), this supports conjecture of the dominant role of fast electrons in the energy transfer to the shock wave generated in a solid target under the absence of the pre-plasma. It is very important, that the K_α emission was not observed for the focal spot radii larger than $R_L = 100$ μm and in the case of the pre-plasma presence. This indicates that the effect of the fast electron energy transfer occurs only when irradiating the targets by higher laser intensities and under the absence of the pre-plasma. On the other hand, this effect is suppressed at the pre-plasma presence.

However, the influence of the pre-plasma on K_α emission is not unequivocal when taking into account the results of 2D simulations presented later in Section 6 and conclusions formulated on their basis (Section 7). They suggest that the pre-plasma presence might lead to enhanced resonant absorption due to the increase of scalelength and better adjusting of the laser rays to the optimal angle (Gus'kov *et al.*, 2014).

According to these conclusions, observation and discussion of Cu K_α images presented in this section should be treated as preliminary results that also require to take into consideration X-ray spectroscopic and fast electron energy measurements for various conditions of irradiation of the two-layer targets. Such experiments are planned for a further stage of SI-related research carried out at PALS.

Table 1. *The comparison of the number of K_α photons for different focus spot radii and various laser energies.*

Shot no.	E_L (J)	R_L (μm)	I_L (W/cm^2)	$N_{K\alpha}$
45525	270	100	2.9E15	2.2E10
45504	290	50	1.2E16	6.1E10
45491	430	50	1.8E16	1.5E11
45499	470	50	2.0E16	1.2E11
45463	590	50	2.5E16	2.9E11

5. ION EMISSION MEASUREMENTS

The ion diagnostics applied in the PALS experiment consisted of the ion collectors which were installed at different angles (from 0° to 60°) at the distance of 40 cm from the target. The collected ion current was emitted from the two-layer targets (see Fig. 1). The sorted results provided by this diagnostic system are presented in Figure 16. In the left column, there are results obtained without the application of the pre-pulse and in the right column the results obtained with the pre-pulse application. The basic difference in the subsequent experimental series is in the focus radius which ranged from 50 to 200 μm. The parameters of the laser beam were at the same level for all experimental series (about 250 J in the main beam and about 40 J in the pre-pulse).

The diagrams show the time dependence of the ion collector signals as the function of time for different angles and focal diameters.

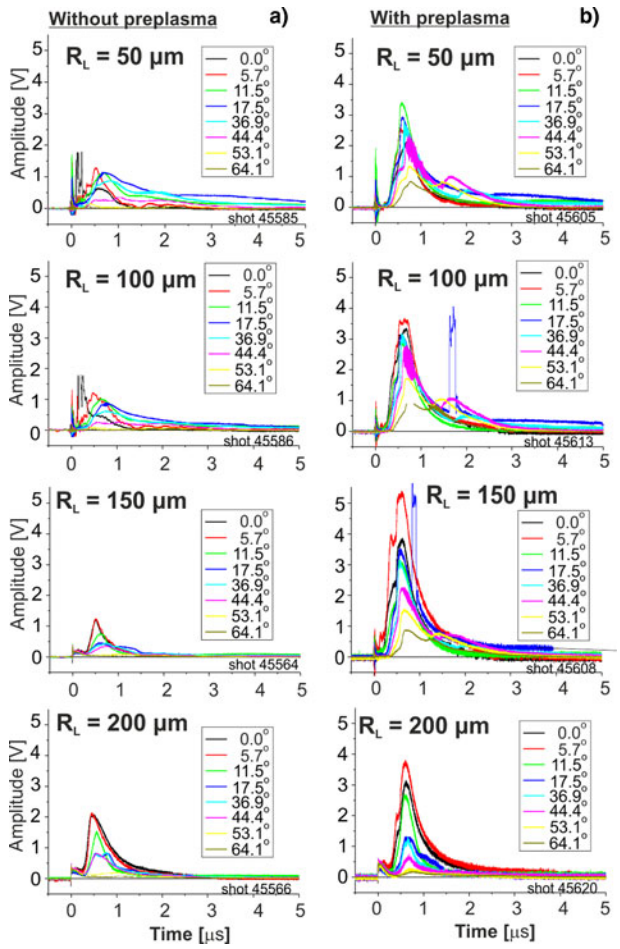

Fig. 16. Oscillograms illustrating temporary changes of the ion collector signals measured at different angles (with respect to the laser beam) and at various focal spot radii of the main laser beam in the case of (a) without and (b) with the pre-plasma.

https://doi.org/10.1017/S0263034615000233 Published online by Cambridge University Press

The main conclusions following from these results may be summarized in several points:

- The number of thermal ions (second delayed peak) in the case of the pre-plasma presence is 2–3 times larger than that observed in the case of the pre-plasma absence for all the beam radii. It means that the absorption coefficient in the case of the pre-plasma presence is 2–3 times larger than in the case of the pre-plasma absence. This conclusion is confirmed by the results of 2DSs presented in the next section.
- In the case of the pre-plasma presence, the fast ions (first peak) are generated at all radii of the laser beam. Since the fast ions are generated in the field of fast electrons, this means that in the presence of the pre-plasma also the fast electrons are generated at all laser beam radii. This conclusion agrees with the results of 2DSs predicting high efficiency of resonant absorption of laser radiation for all radii of the laser beam in the presence of the pre-plasma.
- In the case of the pre-plasma absence, the fast ions are generated only at radii of 100 and 50 μm. It is in agreement with the above-presented results on fast electron generation from interferometric and X-ray spectroscopic measurements.
- The time of the second peak observation is approximately the same for cases with and without the pre-plasma as well as for all radii of the laser beam and equal to about 0.7 μs.
- The time of the first peak observation (0.15 μs) is significantly shorter than that of the second peak which indicates that the energies of fast ions are much larger than those of thermal ions.

The ion collector data non-separated with respect to the ion types give a possibility to determine only the scales of temperature of the plasma plume and average energy of fast electrons. Taking the time of the second peak as 0.7 μs, the average velocity of thermal ions as $(3\,T/2m_p)^{1/2}$ (in the $A/Z = 2$ approximation) and the distance between the target and the collector equal to 40 cm, we obtain the value of plasma temperature, averaged on space and time, which is approximately equal to 2.1 keV. This value is obviously larger than the time-averaged temperature obtained from the X-spectroscopy measurements, since the latter one corresponds to the relatively cold part of the plasma torch near the ablation surface. Now, taking the average velocity of the fast ions as $(E_h/m_p)^{1/2}$ (where the energy of fast ions was, approximately, expressed through the average energy of fast electrons E_h as ZE_h) and the time of second peak as 0.15 μs, we obtain the average energy of fast electrons approximately equal to 70 keV. Figure 17 shows the plots of charge distributions for each experimental series, calculated on the basis of the integration of the charge of both the thermal ions (of time-of-flight ranging in 50–500 ns).

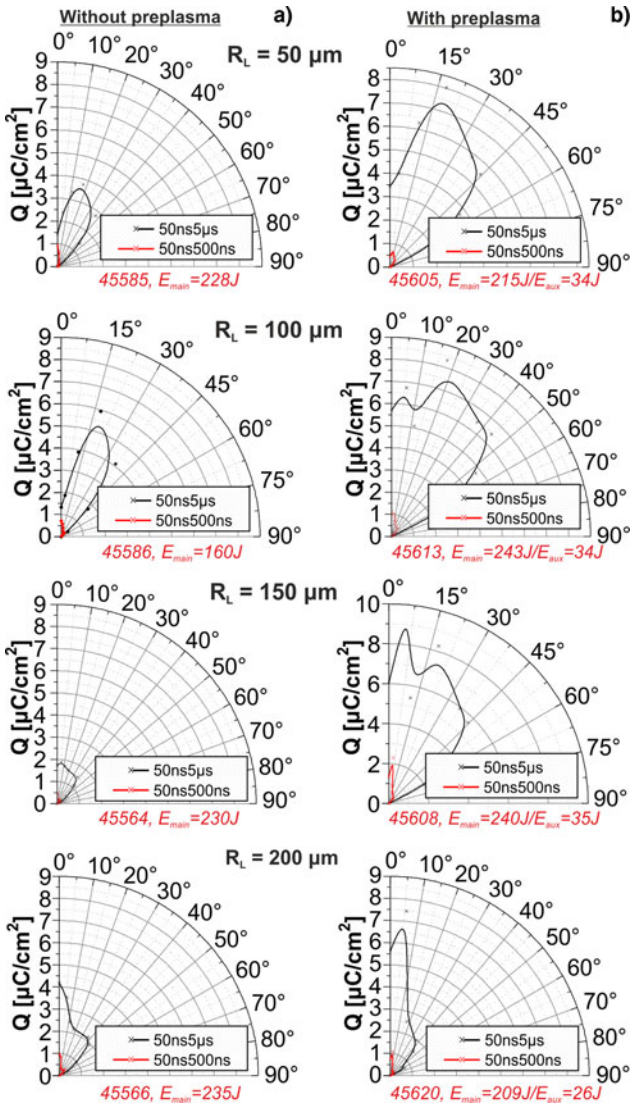

Fig. 17. The angular distribution of the ion charge density for different focal spot radii in the case of (a) without and (b) with the pre-plasma.

When comparing the results from two columns depicted in Figure 17, it can be seen that when increasing the focal diameter, the ions are better collimated which manifests in a distinct plasma "jet". When the pre-pulse configuration is applied together with the 200 μm focus diameter, the jet is well visible and the whole group of the pre-pulse series has considerably larger integrated charges than those obtained without the pre-pulse.

6. NUMERICAL SIMULATIONS AND DISCUSSION

The numerical simulations of the laser beam interaction with the two-layer targets (Fig. 1) were carried out using the 2D hydrodynamic code ATLANT-HE (Lebo *et al.*, 2004). This code includes modeling of the laser radiation refraction in the plasma, inverse bremsstrahlung and resonance absorption of laser radiation, generation of fast electrons due to the

https://doi.org/10.1017/S0263034615000233 Published online by Cambridge University Press

resonance absorption, and the fast electron energy transfer with Coulomb collisions. The aim of the numerical calculations was the acquisition of the information about:

- the temporal evolution of 2D spatial distributions of the density as well as electron and ion temperatures of the laser-produced plasma;
- the fractions of the laser energy absorbed in the plasma by resonant and inverse bremsstrahlung mechanisms;
- energy of fast electrons.

The calculation details are explained in our recent paper (Gus'kov *et al*., 2014). To model the experimental conditions, the computations were performed for the 1ω radiation of the main laser beam with the energy of 250 J and three values of the focal spot radius: 50, 100, and 200 μm. In the case of the two-beam experiment referring to the SI concept, the pre-plasma was created by the auxiliary 1ω laser beam with the energy of 40 J focused to the focal spot radius $R_L = 300$ μm and preceding by 1.2 ns the main laser pulse.

For the case of the pre-plasma absence, the 2D calculations of the density and temperature corresponding to the maximum laser intensity are presented in Figure 18. In contrast to the experimental results shown in Figure 6, these density distributions do not demonstrate the growth of the axial character of the plasma expansion with the increasing focal spot radii. As demonstrated in Figure 18, the growth of the focal spot radius leads to the increased transverse dimension of the ablative plasma.

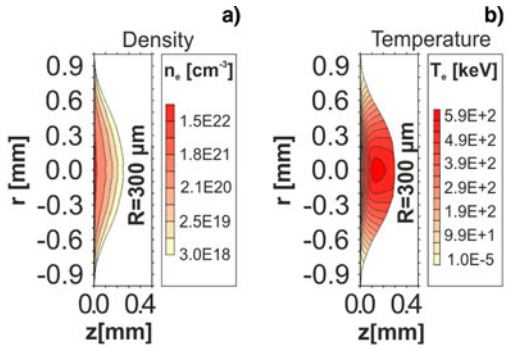

Fig. 19. Distributions of the density (a) and temperature (b) in the pre-plasma for the expansion time $t = 400$ ps.

The distribution of the electron density and temperature of the pre-plasma produced by the auxiliary laser beam is

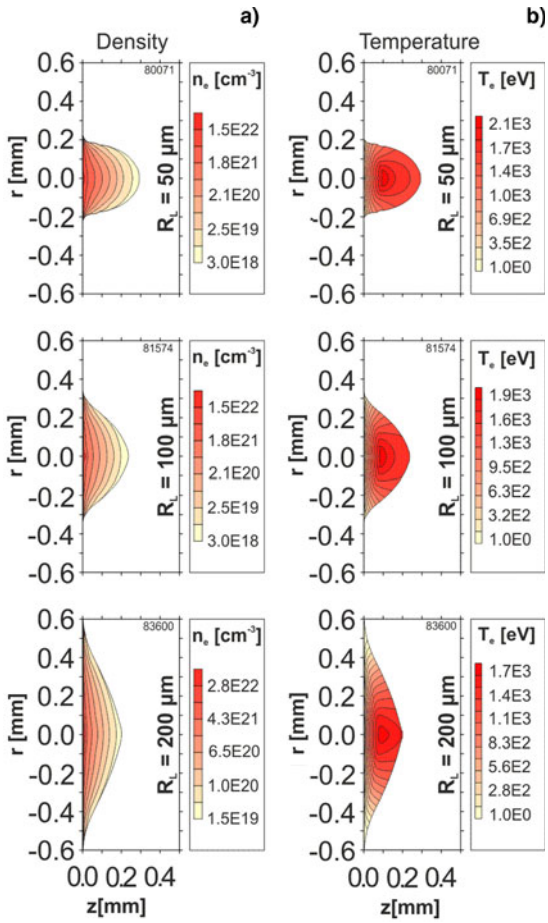

Fig. 18. The density (a) and temperature (b) distributions of the ablative plasma created by the main laser beam at the time of its intensity maximum.

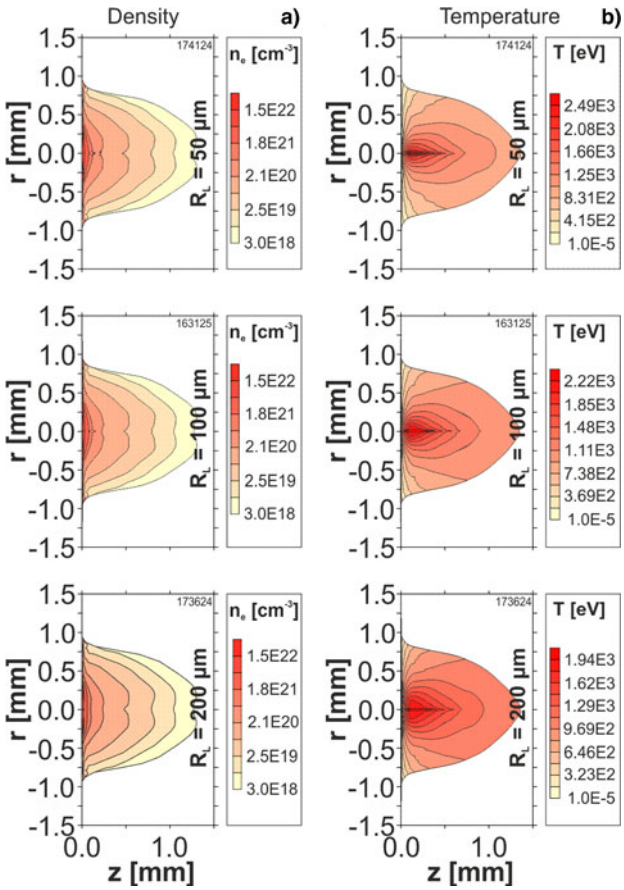

Fig. 20. The density (a) and temperature (b) distribution characterizing the laser interaction with the pre-plasma at the time delay of $t = 1.2$ ns between the auxiliary and the main laser beam.

https://doi.org/10.1017/S0263034615000233 Published online by Cambridge University Press

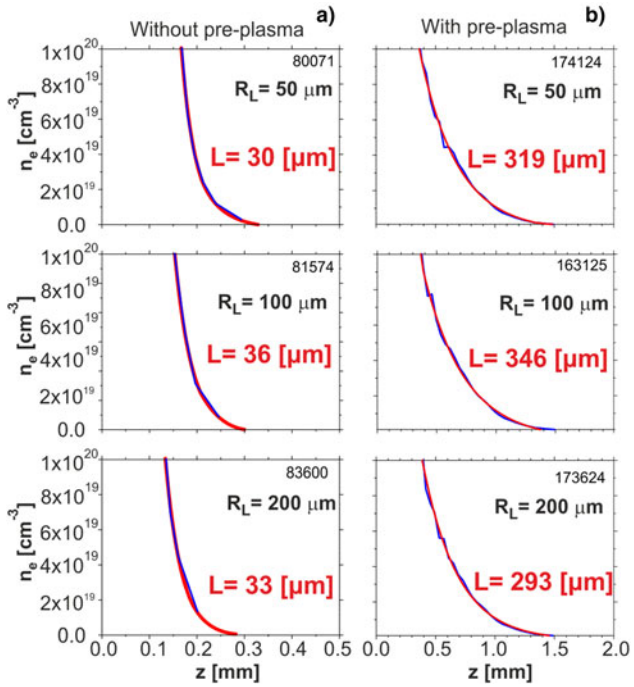

Fig. 21. Comparison of the axial density profiles and the scalelength obtained in the case of (a) absence and (b) presence of the pre-plasma.

shown in Figure 19. This distribution corresponds to time t = 400 ps, that is, to the end of the pulse. The 2D distributions of the density and temperature characterizing the process of the interaction of the main beam with the pre-plasma created by the auxiliary laser beam are presented in Figure 20. These distributions clearly demonstrate the effect of the pre-plasma on the ablative plasma expansion.

The detailed comparison of the axial density profiles and the scalelength in the ablative plasma, both in cases of the pre-plasma absence and presence, is presented in Figure 21. Compared with the situation when the pre-plasma is not created, the scalelength of the ablative plasma is considerably larger. Comparison of the experimental data with the 2DS is presented in Table 2. This comparison has been performed in the range of the electron density smaller than 10^{20} cm^{-3} as determined from the femtosecond interferometry. Table 2 indicates that there is a satisfactory agreement between experimental and numerical data in the case of the pre-plasma presence. In the case of the pre-plasma absence, the qualitative character is the same but the observed and simulated scalelength values differ considerably.

The large values of experimental scalelengths result from the action of the temporally extended beam profile which is characteristic for the PALS laser and contributes to the creation of the low-density plasma even in the case of the pre-pulse absence. A long pedestal (even about 1 ns long) of the pulse is not taken into account in numerical simulations. In the case of the pre-plasma presence, the contribution of the pre-pulse is significantly smaller compared with the pre-plasma itself. This is why the experimental and numerical scalelengths agree well in the case of the pre-plasma presence.

In Table 3, the numerical simulations of the total (δ_a), the resonant [$\delta_{a(r)}$], and the inverse bremsstrahlung $\delta_{a(ib)}$ absorption coefficients are compared for the cases of the pre-plasma absence and presence. This comparison demonstrates the significant larger total absorption coefficient in the case of the pre-plasma presence compared with the case of the pre-plasma absence. The excess is, approximately, the factor of 3 for the beam radius of 50 μm and the factor of 2 for the beam radius of 100 μm. This explains the ion collector measurements, where the number of thermal ions in the case of the pre-plasma presence is by a factor of 2–3 larger in comparison with the case of the pre-plasma absence. The maximal temperature (occurring near the region of the critical density plasma) obtained by numerical simulations falls within the interval of (2–3) keV which agrees well with evaluation based on ion collectors data. The pre-plasma provides better conditions for resonant absorption of the laser energy. For the beam radius of 50–100 μm, the resonant absorption coefficient is equal to $\delta_{a(r)}$ = 0.32–0.23 in the case of the pre-plasma presence and to $\delta_{a(r)}$ = 0.06–0.09 in the case of the pre-plasma absence. The maximal energies of fast electrons are about 140–120 keV. This value relates to the electrons which twice crossed the region of plasma resonance after their reflection from external plasma boundary. These estimates are very close to the values evaluated from ion collector data. This evaluation gives the value of the average fast electron energy 70 keV that corresponds to the maximal energy of 140 keV.

Table 2. *The comparison of the experimental scalelength with the 2DS in the case of the presence and absence of the pre-plasma.*

L (μm)	W/O pre-plasma		W pre-plasma	
R_L (μm)	Exp	2DS	Exp.	2DS
50	125	30	326	320
100	190	36	420	346
200	140	34	365	296

Table 3. *The comparison of the numerical simulations of the total (δ_a), the resonant [$\delta_{a(r)}$] and the inverse bremsstrahlung $\delta_{a(ib)}$ absorption coefficients in the cases of the pre-plasma absence and presence.*

RL (μm)	50		100		200	
	W/O	W	W/O	W	W/O	W
δ_a	0.21	0.64	0.29	0.57	0.42	0.59
$\delta_{a(ib)}$	0.15	0.31	0.19	0.34	0.25	0.39
$\delta_{a(r)}$	0.06	0.32	0.09	0.23	0.17	0.21
$E_{h(max)}$ (keV)	143	152	129	144	121	114
T_{emax} (keV)	2.48	3.27	2.20	2.99	1.92	2.31

https://doi.org/10.1017/S0263034615000233 Published online by Cambridge University Press

According to the numerical modeling presented in (Gus'kov *et al*., 2014), the increased efficiency of the resonance absorption in the case of the pre-plasma results probably from a better fitting of the angles between the individual laser rays and the direction of the density gradient near the critical surface (these angles are closer to optimum angles because of the smaller scalelength).

7. CONCLUSIONS

Summing up the comparison of the experimental and numerical data we can claim that:

- Based on the interferometric results, measurements of the crater volume, spectroscopic determination of the temperature and density near the ablation surface, and imaging via K_α-emission, there is a good reason to conclude that the presence of the pre-plasma leads to the decrease in the energy transfer efficiency of the main 1ω laser beam to a solid target by means of fast electrons. In the same time, 2DSs show that the presence of the pre-plasma makes the conditions of resonant absorption of the laser radiation more favorable, increases the fraction of the laser energy absorbed by resonant mechanism, and hence increases the energy contained in the fast electron stream.
- The results of the interferometric measurements, as well as the results of 2DSs, show that the presence of the pre-plasma decreases the axial density gradient.
- The decrease of the contribution of the fast electron energy transfer to a solid target at the increasing laser energy conversed to fast electrons can be explained by a deterioration of the conditions of energy transfer by fast electrons in the presence of the pre-plasma. There are two reasons of such decline:

  (1) First, the large divergence of streaming fast electrons which are generated far from the target surface in the presence of the pre-plasma.
  (2) Second, the effect of plasma density gradient at the irradiated boundary of target on the efficiency of the energy transfer from fast electrons streaming to the shock wave. Such an effect was predicted and numerically investigated in (Nicolai *et al*., 2014).

ACKNOWLEDGMENTS

This work was supported in part by the Access to Research Infrastructure activity in the 7th Framework Program of the EU Contract No. 284464, Laserlab Europe III, by the Czech Republic's Ministry of Education, Youth and Sports under PALS RI Project (No. LM2010014), by National Centre for Science (NCN), Poland under Grant No. 2012/04/M/ST2/00452, and by the ToIFE Project of the EUROfusion Consortium and by the French-Polish bilateral collaboration program POLONIUM and of the COST Action MP1208 "Developing the physics and the Scientific Community for Inertial Fusion. The participation of S. Yu. Gus'kov and N. N. Demchenko in this work was supported by RFBR Projects No. 14-02-00010 and No. 13-02-00295. The participation of O. Renner and M. Smid was supported by the ASCR Project No. M100101208, the ELI-Beamline Project No. CZ.1.05/1.1.00/02.0061 and MSMT COST CZ Project LD14089, while the participation of J. Dostal was supported by the Grant Agency of the Czech Republic, Project No. P205-11-P712.

REFERENCES

Antonelli, L., Batani, D., Patria, A., Ciricosta, O., Cecchetti, C.A., Koester, P., Labate, L., Giulietti, A., Gizzi, L.A., Moretti, A., Richetta, M., Giuffrida, L., Torissi, L., O'dell, T., Kozlova, M., Nejdl, J., Sawicka, M., Margarone, D., Rus, B., Schurtz, G., Ribeyre, X., Lafon, M. & Spindloe, C. (2011). Laser-plasma coupling in the shock-ignition intensity regime. *Acta Tech. CSAV* **56**, T57–T69.

Batani, D., Antonelli, L., Atzeni, S., Badziak, J., Baffigi, F., Chodukowski, T., Consoli, F., Cristoforetti, G., De Angelis, R., Dudzak, R., Folpini, G., Giuffrida, L., Gizzi, L.A., Kalinowska, Z., Koester, P., Krousky, E., Krus, M., Labate, L., Levato, T., Maheut, Y., Malka, G., Margarone, D., Marocchino, A., Nejdl, J., Nicolai, P., O'DELL, T., Pisarczyk, T., Renner, O., Rhee, Y.J., Ribeyre, X., Richetta, M., Rosinski, M., Sawicka, M., Schiavi, A., Skala, J., Smid, M., Spindloe, C., Ullschmied, J., Velyhan, A. & Vinci, T. (2014a). Generation of high pressure shocks relevant to the shock-ignition intensity regime. *Phys. Plasmas* **21**, 032710.

Batani, D., Baton, S., Casner, A., Depierreux, S., Hohenberger, M., Klimo, O., Koenig, M., Labaune, C., Ribeyre, X., Rousseaux, C., Schurtz, G., Theobald, W. & Tikhonchuk, V.T. (2014b). Physical issues in shock ignition. *Nucl. Fusion* **54**, 054009.

Betti, R., Zhou, C.D., Anderson, K.S., Perkins, L.J., Theobald, W. & Solodov, A.A. (2007). Shock ignition of thermonuclear fuel with high areal density (2007). *Phys. Rev. Lett.* **98**, 155001.

Borodziuk, S., Kasperczuk, A., Pisarczyk, T., Gus'kov, S.Yu., Ullschmied, J., Kralikova, B., Rohlena, K., Skala, J., Kalal, M. & Pisarczyk, P. (2004). Application of laser simulation method for the analysis of crater formation experiment on PALS laser. *Opt. Appl.* **34**, 31.

Burrus, C.S. (2008). *Fast Fourier Transforms*. Connexions, Rice University, Houston, Texas.

Gus'kov, S.Yu., Borodziuk, S., Kalal, M., Kasperczuk, A., Kralikova, B., Krousky, E., Limpouch, J., Masek, K., Pisarczyk, P., Pisarczyk, T., Pfeifer, M., Rohlena, K., Skala, J. & Ullschmied, J. (2004). Generation of shock waves and formation of crater in a solid material irradiated by a short laser pulse. *Quantum Electron.* **34**, 989.

Gus'kov, S.Yu., Demchenko, N.N., Kasperczuk, A., Pisarczyk, T., Kalinowska, Z., Chodukowski, T., Renenr, O., Smid, M., Krousky, E., Pfeifer, M., Skala, J., Ullschmied, J. & Pisarczyk, P. (2014). Laser-driven ablation through fast electrons in PALS- experiment at the laser radiation intensity of 1–50 PW/cm^2. *Laser Part. Beams* **32**, 177–915.

Gus'kov, S.Yu., Kasperczuk, A., Pisarczyk, T., Borodziuk, S., Ullschmied, J., Krousky, E., Masek, K., Pfeifer, M., Skala, J. & Pisarczyk, P. (2007). Energy of a shock wave generated

https://doi.org/10.1017/S0263034615000233 Published online by Cambridge University Press

in different metals under irradiation by a high-power laser pulse. *J. Exp. Theor. Phys.* **105**(4), 793–802.

Gus'kov, S.Yu., Ribeyre, X., Touati, M., Feugeas, J.L., Nicolae, Ph. & Tikhonchuk, V.T. (2012). Ablation pressure driven by an energetic electron beam in a dense plasma. *Phys. Rev. Lett.* **102**, 255004.

Gus'kov, S.Yu., Zverev, V.V. & Rozanov, V.B. (1983). Steady-state model of the corona of spherical targets allowing for energy transfer by fast electrons. *Quantum Electron.* **13**, 498.

Kalal, M. & Nugent, K.A. (1988). Abel inversion using fast Fourier transforms. *Appl. Opt.* **27**, 1956.

Kalinowska, Z., Kasperczuk, A., Pisarczyk, T., Chodukowski, T., Gus'kov, S.Yu., Demchenko, N.N., Ullschmied, J., Krousky, E., Pfeifer, M., Skala, J. & Pisarczyk, P. (2012). Investigations of mechanisms of laser radiation absorption at PALS. *Nukleonika* **57**, 227.

Kasperczuk, A. & Pisarczyk, T. (2001). Application of automated interferometric system for investigation of the behaviour of a laser produced plasma in strong external magnetic fields. *Opt. Appl.* **XXXI**, 571–597.

Koester, P., Antonelli, L., Atzeni, S., Badziak, J., Baffigi, F., Batani, D., Cecchetti, C.A., Chodukowski, T., Consoli, F., Cristoforetti, G., De Angelis, R., Folpini, G., Gizzi, L.A., Kalinowska, Z., Krousky, E., Kucharik, M., Labate, L., Levato, T., Liska, R., Malka, G., Maheut, Y., Marocchino, A., O'DELL, T., Parys, P., Pisarczyk, T., Raczka, P., Renner, O., Rhee, Y.J., Ribeyre, X., Richetta, M., Rosinski, M., Ryc, L., Skala, J., Schiavi, A., Schurtz, G., Smid, M., Spindloe, C., Ullschmied, J., Wolowski, J. & Zaras, A. (2013). Recent results from experimental studies on laser-plasma coupling in a Shock Ignition relevant regime. *Plasma Phys. Controll. Fusion* **55**, 124045.

Lebo, I.G., Demchenko, N.N., Iskakov, A.B., Limpouch, J., Rozanov, V.B. & Tishkin, V.F. (2004). Simulation of high-intensity laser – plasma interactions by use of the 2D Lagrangian code ATLANT-HE. *Laser Part. Beams* **22**, 267–273.

Macfarlane, J.J., Golovkin, I.E., Wang, P., Woodruff, P.R. & Pereyra, N.A. (2007). SPECT3D – A multi-dimensional collisional-radiative Code for generating diagnostic signatures based on hydrodynamics and PIC simulation output. *High Energy Density Phys.* **3**, 181.

Morace, A. & Batani, D. (2010). Spherically bent crystal for X-ray imaging of laser produced plasmas. *Nucl. Instrum. Methods A* **623**, 797.

Nicolai, P., Feugeas, J.L., Toutati, M., Ribeyre, X., Gus'kov, S.Yu. & Tikhonchuk, V. (2014). Deleterious effects of nonthermal electrons in shock ignition concept. *Phys. Rev. E* **89**, 033107.

NIST ESTAR database. http://physics.nist.gov/PhysRefData/Star/Text/ESTAR.html

Scherbakov, V.A. (1983). On the expediency of making double-pulse lasers for laser thermonuclear fusion. *Sov. J. Plasma Phys.* **9**, 240.

Smid, M., Antonelli, L. & Renner, O. (2013). X-ray spectroscopic characterization of shock-ignition-relevant plasmas. *Acta Polytech.* **53**, 233.

Perkins, L.J., Betti, R., La Fortune, K.N. & Williams, W.H. (2009). Shock ignition – a new approach to high gain inertial confinement fusion on the National Ignition Facility. *Phys. Rev. Lett.* **103**, 045004.

Pisarczyk, T., Gus'kov, S.Yu., Kalinowska, Z., Badziak, J., Batani, D., Antonelli, L., Folpini, G., Maheut, Y., Baffigi, F., Borodziuk, S., Chodukowski, T., Cristoforetti, G., Demchenko, N.N., Gizzi, L.A., Kasperczuk, A., Koester, P., Krousky, E., Labate, L., Parys, P., Pfeifer, M., Renner, O., Smid, M., Rosinski, M., Skala, J., Dudzak, R., Ullschmied, J. & Pisarczyk, P. (2014). Pre-plasma effect on energy transfer from laser beam to shock wave generated in solid target. *Phys. Plasmas* **21**, 012708.

Podorov, S.G., Renner, O., Wehrhan, O. & Furster, E. (2001). Optimized polychromatic x-ray imaging with asymmetrically cut bent crystals. *J. Phys. D: Appl. Phys.* **34**, 2363.

Ribeyre, X., Schurtz, G., Lafon, M., Galera, S. & Weber, S. (2009). Shock ignition: modelling and target design robustness. *Plasma Phys. Controll. Fusion* **51**, 015013.

Theobald, W., Betti, R., Stoeckl, C., Aanderson, K.S., Delettrez, J.A., Glebov, V.Y., Goncharov, V.N., Marshall, F.J., Maywar, D.N., Mccrory, R.L., Meyerhofer, D.D., Radha, P.B., Sangster, T.C., Seka, W., Shvarts, D., Smalyuk, V.A., Solodov, A.A., Yaakobi, B., Zhou, C.D., Frenje, J.A., Li, C.K., Siguin, F.H., Petrasso, R.D. & Perkins, L.J. (2008). Initial experiments on the shock-ignition inertial confinement fusion concept. *Phys. Plasmas* **15**, 056306.

Theobald, W., Nora, R., Lafon, M., Casner, A., Ribeyre, X., Anderson, K.S., Betti, R., Delettrez, J.A., Frenje, J.A., Glebov, V.Y., Gotchev, O.V., Hohenberger, M., Hu, S.X., Marshall, F.J., Meyerhofer, D.D., Sangster, T.C., Schurtz, G., Seka, W., Smalyuk, V.A., Stoeckl, C. & Yaakobi, B. (2012). Spherical shock-ignition experiments with the 40 + 20-beam configuration on OMEGA. *Phys. Plasmas* **19**, 102706.

https://doi.org/10.1017/S0263034615000233 Published online by Cambridge University Press